Resistive modes in the edge and scrape-off-layer of diverted tokamaks

J. R. Myra, D. A. D'Ippolito

Lodestar Research Corporation

X. Q. Xu, R. H. Cohen

Lawrence Livermore National Laboratory

July 2000

(submitted to Physics of Plasmas)

DOE/ER/54392-11 LRC-00-79

Resistive modes in the edge and scrape-off-layer of diverted tokamaks

J. R. Myra, D. A. D'Ippolito

Lodestar Research Corp., 2400 Central Ave. P-5, Boulder, Colorado 80301

X. Q. Xu, R. H. Cohen

Lawrence Livermore National Laboratory, Livermore, CA 94550

Abstract

The linear behavior of resistive ballooning modes in the edge and scrape-off-layer of diverted tokamaks is explored in the context of a collisional fluid model. It is shown that the large magnetic shear and small poloidal field in the X-point region act to increase the wavenumber, and hence the importance of resistivity, near the X-point. The resulting "disconnection" of the eigenmodes across the X-point profoundly influences the unstable spectrum. A new class of modes called resistive X-point (RX) modes exploits this synergism between resistivity and the X-point geometry, giving rise to robust growth rates at moderate-to-low mode numbers. Relative to an equivalent limited plasma, the diverted plasma is shown to be more unstable in the edge (inside the separatrix), and more stable in the scrape-off-layer. Implications for the role of X-points on the nonlinear generation of radial electric fields and the transition from low to high (L-H) confinement are discussed.

PACS: 52.55.Fa, 52.35.-g, 52.30.Jb, 52.35.Ra

I. Introduction

The physics of the edge and scrape-off-layer (SOL) continues to be an active area of research because this region of the plasma provides an important, and as yet poorly understood, boundary condition for the hot core of a tokamak plasma. Furthermore, SOL physics is important in its own right as the SOL width controls the heat flux to the divertor plates – a critical issue for tokamak fusion reactor designs. It is generally believed that turbulence in the edge and SOL regions will be an important ingredient of a complete edge physics model.

In this paper, we will examine the role of X-points on the instabilities that exist in the boundary (edge and SOL) plasma. X-point effects influence the attainment of high confinement (H) modes in experiments. While the geometry of the divertor and separatrix importantly affects the plasma equilibrium (e.g. through recycling and the penetration of neutrals and impurities), which may well account for many of the experimentally observed differences between limited and diverted plasma, this paper will show that the boundary plasma turbulence is strongly modified as well.

Our work is related to previous studies[1,2] that have as a goal the understanding of edge turbulence; however, the present study differs in that here we focus on the fundamental role of the X-point and SOL. X-point effects on both waves[3-5] and instabilities[6-12] have been treated previously in the literature. A review of this work, with a more complete bibliography, is given in Ref. 13. The unique feature of the present study, and of companion work using the BOUT code,[14,15] is the identification of modes with a strong *localized* X-point interaction. Our paper supplements and extends an earlier paper[16] in which some of the basic ideas underlying the "resistive X-point mode" were presented.

To address questions about the role of separatrix geometry on boundary plasma turbulence, several tools have recently been developed. The BOUT code[14,15] is a three-dimensional turbulence code which models both the edge plasma and SOL regions. The BAL code, an extension of the code described in Ref. 11, is a companion linear eigenvalue code that is used to further elucidate the physics of the modes. Both codes employ realistic magnetic separatrix geometry and plasma parameters.

The present paper will describe the linear BAL code results and their physical interpretation. The work is motivated, in part, by recent nonlinear BOUT simulations which have been able to make contact with experimental observations in several important ways. In one type of simulation, a fixed profile analysis using experimental data in low (L) and high (H) confinement modes from the DIII-D tokamak, it was shown that fluctuations and transport are suppressed in the H-mode.[15] These realistic parameter simulations also led to first-principles calculations of the cross-field thermal diffusivity in L and H phases which were in reasonable absolute agreement with experimental analysis.

In more recent work, source and sinks have been added to BOUT enabling the simulation of a dynamical L-H transition.[14] It was found that heating triggered the transition to a better confinement state in which the heat flux dropped dramatically. The reduction of transport was attributed to turbulent suppression by the self-generated flow shear. These successes in modeling experiments give some confidence in the basic physical models being employed and motivate further study of their properties.

There are several features of the BOUT simulations which linear theory must explain. First is the basic nature of the instabilities – their fundamental drives and dependence on parameters and geometry. Another is the similarity of the fluctuations in the edge and SOL in the L-phase. For example, the L-phase curve showing fluctuation amplitudes in Fig. 4a of Ref. 15 has nearly even parity about a point close to the separatrix. (The symmetry is somewhat broken in the H-phase by the development of

strong flow shear inside the separatrix.) This symmetry is initially surprising, since naively one would expect the different boundary conditions on the edge and SOL field lines to dramatically affect the mode behavior. Finally, the BOUT simulations typically show that fluctuations, such as the electrostatic potential or density perturbation, are strongly localized between upper and lower X-points on the bad curvature side of the torus. While the usual ballooning effect could be expected to concentrate modes to the bad curvature region, the effect seen is much stronger, and occurs for L-mode parameters for which the ballooning effect should be weak.

The goal of the present paper is to address these questions about the basic nature of the fluctuations, the relationship of the edge to the SOL, and the role of X-points in mode localization. We will see that resistivity and X-point geometry are synergistic, that X-point geometry strongly affects modes for realistic cases, and that the stability properties of the SOL have an interesting role in our overall understanding of boundary plasma physics.

The plan of our paper is as follows. In Sec. II we review the most important features of wave physics in X-point geometry. Starting from a reduced Braginskii set of equations, Sec. III contains an analytical derivation of the ballooning equation and associated boundary conditions for drift-resistive modes. In Sec. IV, we present numerical results from the BAL code illustrating the basic physics of resistive modes in X-point geometry, and a comparison of edge and SOL instabilities in divertor and limiter configurations. Conclusions are given in Sec. V. In Appendix A the limiting cases of large and small parallel thermal conductivity are considered in the linearized electron response. Finally, in Appendix B, the ion gyrokinetic model is derived for use in the gyrokinetic-fluid comparisons presented in Sec. IV A.

II. Wave physics in X-point geometry

Before proceeding with a detailed examination of specific unstable modes in the edge and SOL plasma in divertor geometry, we will consider some general consequences of an X-point on wave propagation. The dominant effects are:[13]

(i) k_θ increases locally in the X-point region as a result of the null in B_θ.

(ii) Strong magnetic shear near the X-point leads to an integrated increase of k_ψ.

(iii) Field lines linger near the X-point affecting the curvature weighting of modes.

(iv) The X-point increases connection lengths, which reduces $k_\parallel$ and line bending energy, and, in the SOL, increases the connection length to the plates (making the plate boundary conditions of less importance).

Here, our orthogonal coordinate system is (ψ, θ, ζ) = ("radial", poloidal, toroidal). The first two points are the most important ones for this paper. Point (iii) has been treated in Refs. 6 and 7, and leads to the result that the X-point should be placed in a region of neutral or good curvature for optimum stability of the configuration. Point (iv) is discussed in Ref. 8. Here we consider points (i) and (ii) in more detail.

Since $k_\parallel$ tends to be much smaller than $k_\perp$ for the modes of interest, the perpendicular eikonal approximation yields the lowest order relationship

$$\mathbf{k}\cdot\mathbf{B} = 0 = k_\theta B_\theta + k_\zeta B_\zeta , \tag{1}$$

or

$$k_\theta = -\frac{nB_\zeta}{RB_\theta}, \tag{2}$$

where n is the toroidal mode number. Thus k_θ is singular where B_θ vanishes.

The effect of magnetic shear can be seen by noting that in the eikonal approximation $\mathbf{k} = \nabla S$ for some eikonal function S. Consequently, $\nabla \times \mathbf{k} = 0$ pertains, and in particular the $\mathbf{e}_\zeta$ component yields a relationship between k_ψ and k_θ,

$$\frac{\partial}{\partial \theta}\left(\frac{k_\psi}{R B_\theta} \right) = \frac{\partial}{\partial \psi}(J B_\theta k_\theta), \tag{3}$$

which may be integrated to obtain an expression for k_ψ. Here J is the Jacobian with $|\nabla\theta| = (JB_\theta)^{-1}$ and the constant of integration may be expressed in terms of the conventional ballooning parameter θ_0. The fact that k_ψ is induced by magnetic shear is well known, and occurs in any tokamak geometry (even for circular flux surfaces). The point here is that the local magnetic shear near an X-point can be very large. The local shear parameter s ($s \equiv d \ln \nu / d \ln \psi$ where ν is the local rotational transform) can typically be as large as 40 at one gyroradius from the X-point. The physics here is the same as in the standard eikonal ballooning formalism, but the consequences of large localized changes in $k_\perp$ will be very significant for the modes.

The variation of k_θ and k_ψ along a field line for a single null X-point geometry (see Ref. 11 for details of the X-point model) is shown in Fig. 1 for a sample flux surface in the SOL (ψ = 103%). The figure is not substantially different in the edge plasma since the magnetic geometry in the vicinity of the X-point is the same just inside and just outside the separatrix. The k_θ component exhibits a local singularity at the X-point because of the null in B_θ, while k_ψ experiences integrated increases near and beyond the X-point as a result of the magnetic shear. The constant arising from integration of Eq. (3) may be chosen to specify the point $\theta = \theta_0$ at which $k_\psi = 0$. In this and subsequent figures, the outside of the torus is at $\theta = \pi/2$ and the lower X-point is at $\theta = 0, 2\pi$.

The geometry-induced variation of k can have a profound effect on the eigenmode structure. As noted by Farina et al.,[3] the appearance of large k (shorter space scales) implies an increased role for resistive and finite Larmor radius (FLR) effects, and

ultimately a disconnection of modes across the X-point region. A rigorous ballooning mode equation describing the wave physics along a field line will be developed in Sec. III.

An example, anticipating the kinds of effects that can occur, is shown in Fig. 2 for the same single-null divertor geometry as in Fig. 1. The figure illustrates the variation of $k_\perp^2$ along a field line (top) and corresponding eigenfunctions (bottom) for three cases, showing progressive disconnection because of resistive X-point effects. The first case (solid) is ideal MHD (resistivity is suppressed by taking $Z_{eff} = 0$) on a field line 2.8 cm from the separatrix in the SOL. It shows that the eigenfunction penetrates the X-point region and continues on to the plates. In the second case (dashed) resistivity is restored ($Z_{eff} = 2$). Still at 2.8 cm from the separatrix, the mode bends only slightly in the X-point region. The third case (dotted) has the same resistivity but is on a field line closer (1.0 cm) to the separatrix. In this case, the synergism between X-point geometry and resistivity is strong enough to cause large line bending and complete disconnection of the mode across the X-point region. This eigenfunction does not "see" the plate, and hence is insensitive to the boundary conditions applied at the plate.

Although this illustration is for the SOL, similar disconnection also occurs in the edge region. This physics and its consequences for the stability of resistive L-mode tokamak boundary plasmas, and ultimately for the L-H transition, is the main subject of the present paper.

III. Analytical derivation

A. Basic equations

The basic equations employed here are a simplified Braginskii fluid model appropriate for the typically collisional boundary plasma. The reduced Braginskii

equations for the potential Φ, parallel current $J_{||}$, density n_e, electron temperature T_e and parallel vector potential $A_{||}$ are given by the vorticity equation, Ohm's law, the continuity equation, the electron temperature (energy) equation and Ampere's law:

$$\frac{c^2}{4\pi v_A^2}\left(\frac{\partial}{\partial t}+\mathbf{v}_E\cdot\nabla+\mathbf{v}_{di}\cdot\nabla\right)\nabla_\perp^2\Phi = B\nabla_{||}\frac{J_{||}}{B}+\frac{2c}{B}\mathbf{b}\times\boldsymbol{\kappa}\cdot\nabla p \tag{4}$$

$$\eta_{||}J_{||}+\frac{\partial}{\partial t}\left(\frac{J_{||}m_e}{n_e e^2}\right)+\nabla_{||}\Phi+\frac{1}{c}\frac{\partial A_{||}}{\partial t}=\frac{1.71}{e}\nabla_{||}T_e+\frac{T_e}{en_e}\nabla_{||}n_e \tag{5}$$

$$\left(\frac{\partial}{\partial t}+\mathbf{v}_E\cdot\nabla\right)n_e=\frac{B}{e}\nabla_{||}\frac{J_{||}}{B}+\frac{2c}{eB}\mathbf{b}\times\boldsymbol{\kappa}\cdot\left(\nabla p_e-n_e e\nabla\Phi\right) \tag{6}$$

$$\frac{3}{2}n_e\left(\frac{\partial}{\partial t}+\mathbf{v}_E\cdot\nabla\right)T_e=\nabla_{||}n_e\chi_{||}\nabla_{||}T_e \tag{7}$$

$$\nabla_\perp^2 A_{||}=-\frac{4\pi}{c}J_{||} \tag{8}$$

where $\mathbf{v}_E=(c/B)\mathbf{b}\times\nabla\Phi$, $\mathbf{v}_{di}=(c/n_e eB)\mathbf{b}\times\nabla p_i$, $v_A{}^2 = B^2/4\pi n_e m_i$, $p = p_e + p_i$, m_e and m_i are the electron and ion masses, $\boldsymbol{\kappa} = \mathbf{b}\cdot\nabla\mathbf{b}$, $\mathbf{b} = \mathbf{B}/B$, $\nabla_{||} = \mathbf{b}\cdot\nabla$, $\eta_{||}$ is the Spitzer parallel conductivity and $\chi_{||}$ is the classical electron parallel thermal diffusivity. The dynamics of the ion temperature and the parallel velocity are neglected. A proper treatment of the ion temperature modifies the nonlinear form of the left-hand-side of Eq. (4),[17] but the linearized equation considered here is unaffected. Neglect of the parallel velocity can be justified *a posteriori* by the large growth rates $\gamma > k_{||}\, c_s$, where c_s is the sound speed. Equation (7) is a simplified electron temperature equation which neglects curvature terms arising from $T_e\nabla\cdot\mathbf{v}$ and perpendicular heat fluxes, and energy exchange terms arising from parallel currents and flows. It will be seen that the linear physics of the modes under consideration here are not very sensitive to the electron temperature model.

Although a more complete set of Braginskii equations is used in the BOUT code modeling,[15] the present set captures the essential linear physics of ideal and resistive magnetohydrodynamics (MHD), and drift waves.

The linearized equations for vorticity, Ohm's law (combined with Ampere's law), continuity, and electron temperature give the following solutions for the perturbed quantities $n_1 = \delta n_e/n_e$, $\phi_1 = e\delta\Phi/T_e$, $T_1 = \delta T_e/T_e$ and $J_1 = \delta J_\parallel/n_e e v_A$ in the high mode number limit ($k_\perp L_\perp >> 1$ where $L_\perp$ is a perpendicular equilibrium scale length)

$$(\tilde{\omega} - \omega_{*i})k_\perp^2\rho_s^2\phi_1 - \omega_\kappa n_1 - \omega_{\kappa e}T_1 + iv_A\nabla_\parallel J_1 = 0 \tag{9}$$

$$(\omega - \omega_{Re} + i\omega_\eta + \tilde{\omega}H)J_1 = -iv_A k_\perp^2\rho_s^2\nabla_\parallel[\phi_1 - n_1 - 1.71T_1] \tag{10}$$

$$(\tilde{\omega} - \omega_{\kappa i})n_1 + (\tilde{\omega} - \omega_{*i})k_\perp^2\rho_s^2\phi_1 - (\omega_{*en} + \omega_{\kappa e})\phi_1 = 0 \tag{11}$$

$$\tilde{\omega}T_1 - \omega_{*eT}\phi_1 = i\nabla_\parallel\frac{2}{3}\chi_\parallel\left(\nabla_\parallel T_1 - \frac{i\omega_{*eT}}{v_A k_\perp^2\rho_s^2}J_1\right) \tag{12}$$

where the following symbols have been defined:

$$\tilde{\omega} = \omega - \omega_E \tag{13}$$

$$\omega_E = \mathbf{k}\cdot\mathbf{v}_E \tag{14}$$

$$\omega_{Re} = \omega_E + \omega_{*en} + 1.71\omega_{*eT} \tag{15}$$

$$\omega_{*en} = -\frac{cT_e}{n_e eB}\mathbf{k}\cdot\mathbf{b}\times\nabla n_e \tag{16}$$

$$\omega_{*eT} = -\frac{c}{eB}\mathbf{k}\cdot\mathbf{b}\times\nabla T_e \tag{17}$$

$$\omega_\eta = \eta_\parallel k_\perp^2 c^2/4\pi \tag{18}$$

$$H = k_\perp^2 c^2/\omega_{pe}^2 \tag{19}$$

$$\omega_{*i} = \mathbf{k}\cdot\mathbf{v}_{di} \tag{20}$$

$$\omega_{\kappa i} = \frac{2cT_i}{eB}\mathbf{k}\cdot\mathbf{b}\times\boldsymbol{\kappa} \tag{21}$$

$$\omega_{\kappa e} = \frac{2cT_e}{eB}\mathbf{k}\cdot\mathbf{b}\times\boldsymbol{\kappa} \tag{22}$$

$$\omega_{\kappa} = \omega_{\kappa i} + \omega_e \tag{23}$$

B. Ballooning equation and boundary conditions

The preceding linearized equations can be combined to obtain a ballooning equation for the modes. A second order differential equation in $\nabla_{\|}$ can be obtained in the limits $\chi_{\|}$ = 0 and $\chi_{\|}$ = ∞. We first consider $\chi_{\|}$ = 0; the other case is treated in Appendix A where it is shown that the $\chi_{\|}$ = 0 limit applies when $k_{\perp}^2\rho_s^2$, H, $\omega_\eta/\omega << 1$ as well as when $k_{\|}^2\chi_{\|}/\omega << 1$. The resulting ballooning equation is

$$B(\omega-\omega_{dkp})\frac{v_A^2}{k_\perp^2}\nabla_{\|}\frac{k_\perp^2/B}{\omega-\omega_{Re}+i\omega_\eta+\tilde{\omega}H}\nabla_{\|}\psi + [\gamma_{mhd}^2+(\tilde{\omega}+\omega_{\kappa e})(\tilde{\omega}-\omega_{*i})]\psi = 0 \tag{24}$$

where

$$\omega_{dkp} = \omega_{Re} + \omega_{\kappa i} - (\tilde{\omega}-\omega_{*i})k_\perp^2\rho_s^2 \tag{25}$$

$$\gamma_{mhd}^2 = -\frac{\omega_\kappa(\omega_{*en}+\omega_{*eT}-\omega_{*i})}{k_\perp^2\rho_s^2(1+T_i/T_e)} \tag{26}$$

and the eigenfunction ψ is

$$\psi = \phi_1 - n_1 - 1.71T_1. \tag{27}$$

In Eq. (24) we have made the nonessential but simplifying assumption of neglecting parallel variations in the equilibrium n_e,T profiles, and some perpendicular compressibility terms associated with $\omega_{\kappa e}$ in Eq. (11).

Equation (24) contains line bending ($\propto \nabla_{\|}^2$), curvature drive ($\propto \gamma_{mhd}^2$) and inertial terms and includes three basic types of waves: the two Alfvén waves (both propagation directions) and the electron drift wave (contained in the ω_{dkp} and ω_{Re} terms). For MHD type modes, resistivity and electron inertia, described by the ω_η and H terms, reduce the line bending term as usual, but in X-point geometry this reduction is highly localized because of the dependence on $k_\perp^2$.

Equation (24) is to be supplemented by periodic boundary conditions in the edge plasma applying the usual ballooning formalism, and by sheath boundary conditions[18,19] at the divertor plates in the SOL which match the current of the wave to the sheath current.

$$\delta J_{\|sheath} = \delta J_{\|}. \tag{28}$$

Explicitly, this yields

$$c_s\left(\phi_1 - \frac{e\Phi}{T_e}T_1\right) = -\sigma v_A J_1 \tag{29}$$

where $\sigma = \mathbf{b}\cdot\mathbf{n}/|\mathbf{b}\cdot\mathbf{n}| = \pm 1$ at each plate, with $\mathbf{n}$ the unit normal vector of the plate pointing in the direction of the plasma. On expressing the boundary condition in terms of ψ one obtains

$$\omega c_s \psi = i\sigma v_A^2 k_\perp^2 \rho_s^2 \frac{\omega - \omega_{dkp}}{\omega - \omega_{Re} + i\omega_\eta + \tilde{\omega}H}\nabla_{\|}\psi \tag{30}$$

where use has been make of the relationship between the sheath potential and temperature at the sheath entrance, viz. $\omega_E + (e\Phi/T_e)\omega_{*eT} = 0$. Important limiting cases of Eq. (30) are the insulating and line-tying (perfectly conducting) limits, respectively $\nabla_{\|}\psi = 0$ and $\psi = 0$, the latter pertaining at sufficiently low mode numbers such that $k_{\|} v_A^2 k_\perp^2 \rho_s^2 << \omega c_s$.

When the field lines do not intersect the divertor plates at normal incidence, there can be additional terms present in the boundary condition. In particular, in the case of glancing incidence, which is typical for diverted tokamaks, there are additional terms arising from cross-field flows and from the change in flux tube length during interchange-type perturbations.[20,21] Treatment of these effects will be deferred to a later study.

Equations (24) and (30) are the key results of this section. The eigenvalue problem they specify describes sheath (i.e. conducting wall), drift, resistive, and ideal magnetohydrodynamic (MHD) ballooning modes in the high-n limit. The assumption of neglecting parallel variations in the equilibrium n_e and T profiles excludes the axial shear mode from this study.

IV. Numerical results

Resistive X-point modes

The solution of the ballooning equation, Eq. (24), in X-point geometry gives rise to modes that capitalize on the synergism between resistivity and X-point geometry. We call these modes resistive X-point (RX) modes. In this section, solutions for these modes will be presented for a realistic magnetic geometry taken from EFIT[22] code runs for a particular discharge on the DIII-D[23] tokamak. Parameters, unless otherwise noted, correspond to those of the L-phase of the discharge, where the effects of E×B shear on the modes are negligible and the plasma is well into the MHD stability regime. At the separatrix, the parameters are: $n_e = 1.86 \times 10^{13}$ cm^{-3}, $T_e = 67$ eV, $T_i = 53$ eV, and the gradient scale lengths are $L_n = 2.3$ cm, $L_{Te} = 1.0$ cm, $L_{Ti} = 2.6$ cm.

An example is give in Fig. 3 which shows the normalized resistive frequency $|\omega_\eta/\omega|$ along a field line (note the logarithmic scale) and the corresponding eigenfunction (solid) and Poynting flux (dotted) for an RX mode in the edge plasma.

The dominant X-point is the lower one at $\theta = 0$ but the effects of the upper X-point at $\theta = \pi$ (actually in the vacuum region) are also evident. Near the outboard midplane, $|\omega_\eta| < |\omega|$ pertains: the mode has the characteristics of an ideal MHD mode and acquires bad curvature drive. Near and beyond the X-points, we have $|\omega_\eta| > |\omega|$ and the mode transitions to an electrostatic resistive mode. In this case, strong line bending becomes energetically feasible, and the mode decays rapidly, avoiding the good curvature region on the inboard side of the torus. The Poynting flux shows propagation of wave energy away from the outboard midplane (where the free energy is supplied) towards the X-points where the energy is absorbed.

The behavior illustrated in Fig. 3 for the edge plasma inside the separatrix is essentially similar to that seen in the SOL, and discussed with Fig. 2. Disconnection across the X-point occurs in both the edge and SOL. Consequently, *in the presence of strong X-point effects, the edge and SOL become similar*: the different boundary conditions that would otherwise apply to the field lines in the edge and SOL become irrelevant in the neighborhood of the separatrix.

Having looked at sample eigenfunctions in detail, we are in a position to step back and examine the full spectrum. Figure 4 shows a typical unstable spectrum (growth rate vs. toroidal mode number) again for L-mode parameters. For $n \sim 50$ there are two spectral peaks which correspond to RX modes. The dominant RX mode (largest growth rate for $n < 100$) has an eigenfunction that peaks near the lower ($\theta = 0$) X-point, while the subdominant low-n branch that maximizes at nearly the same n has an eigenfunction that peaks near the upper ($\theta = \pi$) X-point.

The high-n spectral peak near $n \sim 250$ with $\gamma \sim 200 \times 10^3\ s^{-1}$, is the classical resistive ballooning mode.[24] The corresponding eigenfunction is much more localized near the outboard midplane and relatively insensitive to the presence of the X-points.

Finally, the complicated spectral signatures that appear for $\gamma < 50 \times 10^3$ s^{-1} are associated with the drift-Alfvén modes. When curvature terms are artificially suppressed, the spectral peaks associated with the RX and classical modes disappear, but the drift-Alfvén unstable spectrum remains. Drift-Alfvén coupling becomes important when $\omega_e > \omega_A$ which occurs for $n > 100$ here.

In general, as n increases, the effects of resistivity change. At low n, for the RX mode, resistivity is only significant at the X-points. As n increases, resistivity becomes important along more of the field line, and consequently the modes are increasingly more localized to the outboard midplane.

X-point effects together with resistivity permit a robust instability at relatively low mode numbers. The mixing length argument is suggestive that this RX mode is important for transport because it is a low-n mode and $D \sim \gamma/k^2$. Thus, linear theory suggests that the RX mode is fundamental to the boundary plasma of a diverted tokamak in the resistive L-phase, and this is confirmed by the nonlinear simulations.[14,15]

Finally, from the spectrum for a particular parameter set, we can step back further and examine the general behavior of modes in the parameter space of edge density and temperature. The corresponding growth rate scaling is illustrated in Fig. 5 on a flux surface 0.9 cm inside the separatrix (at the midplane). These computations were performed in the $\chi_{\|} \to \infty$ model (see Appendix A); however, the points we wish to emphasize are generic to the role of resistivity in divertor geometry. Base case parameters for the DIII-D L-phase were used, except for n_e and $T = T_e = 2T_i$. First note that growth rates increase dramatically in the upper right corner of the plot. This is the regime of ideal MHD ballooning instability.

Consider the inset eigenfunctions beginning with the upper left corner. At high T and low n_e the resistivity is weakest. In this regime, the X-point effects are the most dramatic. The eigenfunction illustrates that the resistivity is dominant near the X-points

allowing the mode to plummet rapidly. In this extreme case, the mode survives past the upper and lower X-points and does weakly sample the inside of the torus. At lower T, where resistivity is stronger, the mode is entirely confined by the X-points, but the growth rate is reduced because of the reduced pressure drive. At low T and high n_e one enters the resistive strong ballooning regime. In this case, ballooning of the eigenfunction at the outboard midplane reduces the importance of X-point effects. Finally, at high n_e and T, the plasma becomes unstable to ideal modes, and again is insensitive to the X-point effects. In general, moving along the low-n_eT to high-n_eT diagonal, the growth rates increase and the mode numbers of the most unstable modes decrease.

Thus, the parameter space of Fig. 5 is broadly divided into three regimes: ideal strong ballooning, resistive strong ballooning and resistive X-point. X-point effects are important over a substantial range of parameters.

It is clear that the large enhancements of $k_\perp$ that occur near the X-point will lead to the breakdown of fluid theory when $k_\perp \rho_i \sim 1$. Next, we investigate how such considerations affect the existence of the RX mode and its properties. To this end, a gyrokinetic ion model is derived in Appendix B. It effectively makes the replacement

$$(\tilde{\omega} - \omega_{*i}) k_\perp^2 \rho_s^2 \rightarrow k_\perp^2 \rho_s^2 \left[(\tilde{\omega} - \omega_{*in})(1 - \Lambda_0)/b - \omega_{*iT}(\Lambda_0 - \Lambda_1) \right] \qquad (31)$$

in Eqs. (9) and (11), where $b = k_\perp^2 \rho_i^2$ and the Λ_n (Bessel type) functions are defined in the appendix.

A comparison of the unstable spectra for the fluid limit ($b << 1$) and full ion gyrokinetic model is shown in Fig. 6. In this figure we have considered a field line just inside the separatrix where the enhancement of $k_\perp$ is the strongest, and taken the simplest electron thermal model, $T_1 = 0$. From Fig. 6 it is seen that there are quantitative changes to the growth rates. The high-n modes are suppressed relative to low-n in the full gyrokinetic case. The low-n ($n < 50$) spectrum is relatively unaffected.

The eigenfunctions (not shown) of the fastest branch for $n < 50$ are essentially the same in the fluid and gyrokinetic model. For larger n, some differences occur, but the qualitative and distinctive features of the RX mode remain; namely, the modes exist, the X-points tend to localize the modes to the bad curvature region, and the electrostatic potential peaks just before the mode encounters the X-point. The ion Larmor radius effects on all modes are mitigated by the fact that the eigenfunctions tend to avoid the X-point region.

Finally, to complete the general discussion of RX mode properties, we consider the scaling of the growth rate with curvature κ, collisionality ν_e (or equivalently resistivity $\eta_{||}$), and electron beta β_e (or inverse skin depth squared, where $\beta_e = \rho_s^2 / \delta_e^2$). Results are illustrated in Fig. 7. The curvature scaling plot a) shows that the RX mode (lower solid curve) is curvature driven and is stabilized when curvature is suppressed. In the case of the classical mode, the growth rate decreases until the mode becomes mixed with the drift-Alfvén spectrum, which persists when curvature is turned off. The scaling with collisionality shows that the modes are insensitive to resistivity when it is not too large. At zero resistivity, electron inertia (the collisionless skin effect) effectively takes over the role of resistivity. The electron beta scaling plot shows that when both resistivity and electron inertia are suppressed (the high β_e or ideal MHD case) the modes are stabilized because of the increased weighting of the line bending term. These same qualitative trends in scaling have been observed with the BOUT code.[15]

B. Comparison of divertor and limiter geometries

The importance of the resistive X-point effects is perhaps best illustrated by contrasting the behavior of a diverted plasma with a limited one. We have modeled a limited plasma using the "shifted circle" flux geometry model, taking equal plasma parameters for the two models at the outboard midplane. Figure 8 shows that the two

unstable spectra have important differences. From Fig. 8 a), the X-point is seen to be destabilizing in the edge. This is because the X-point geometry allows RX modes, whereas without an X-point (limited or circle case) the mode is forced to average over both good and bad curvature regions. The X-point has the opposite effect in the SOL, Fig. 8 b), where it is stabilizing. The disconnection effect, which isolates the modes from the plates, prevents sheath driven modes in X-point geometry while they are allowed and can be strong in a limited plasma. These points will be expanded upon subsequently.

Comparing the growth rates of the low-n instabilities in the four combination of edge, SOL, limited (o) and diverted (x), the edge plasma in the circular limited plasma is the most stable, the edge and SOL are similar in a diverted plasma, and the SOL in a limited plasma is the most unstable, viz.

$$\gamma^{O}_{edge} < \gamma^{X}_{edge} \sim \gamma^{X}_{SOL} < \gamma^{O}_{SOL} . \qquad (32)$$

The reason for this ordering of the growth rates in the edge is more clearly evident from an examination of the corresponding eigenfunctions in Fig. 9. It is evident that the X-points confine the eigenfunctions to the bad curvature region, and this generally results in the larger edge growth rate for the diverted plasma case.

The same X-point physics is operative in the SOL, but the consequences of the disconnection are quite different. The edge and SOL are similar in the *divertor* case. However, the edge and SOL are very different in the *limiter* case. Without an X-point, the SOL modes connect to the limiter, allowing the sheath boundary condition to come into play. This often allows robust instabilities. For the curvature driven modes, the sheath boundary condition is very destabilizing when it is in the insulating limit.[25] The insulating limit allows an interchange mode that "sees" only bad curvature. In general, the sheath boundary condition, Eq. (30), is in a partially conducting limit which permits sheath instabilities such as the "conducting wall mode" (or sheath grad-T_e

instability)[11,18,19] which grow as a results of the finite sheath impedance. In addition, the SOL, like the edge, is subject to instabilities of the drift-Alfvén type.

We digress briefly to explore the nature of the modes that gives rise to the large growth rates γ_{SOL}^{O}. The relative contributions of each instability drive in the SOL have been explored by artificially suppressing curvature and/or diamagnetic electron drifts (which control the drift-Alfvén modes) and changing the boundary conditions from the base case (nominal DIII-D like L-mode parameters, but for the limited plasma case). Note that in the form in which the boundary condition is specified by Eq. (30), suppressing diamagnetic electron drifts does not suppress the sheath driven "conducting wall" instability. The base case growth rate in units of γ_{mhd0} (γ_{mhd} evaluated at the outboard midplane) was 0.42. When curvature terms were suppressed, the growth rate dropped to 0.33. With curvature still off, but further artificially replacing the full boundary condition by an insulating one, the growth rate dropped to 0.28, while with a fully conducting (line tied) boundary condition, the growth rate was 0.25. These runs illustrate the sensitivity of the mode to the boundary condition, and the fact that curvature is one, but not the only, instability drive in the SOL. With the full sheath boundary condition, but both curvature and electron drift terms suppressed the growth rate was still finite at 0.07, owing to the sheath-driven instability. Finally, when the sheath boundary condition in this last case was replaced by an insulating one all modes were stable.

We conclude that although the "conducting wall" sheath drive term is not very strong for these parameters, sheath boundary conditions play a crucial role: they enable the drift-Alfvén and curvature driven modes in limiter geometry to be much stronger in the SOL than in the edge. For example, in the insulating limit, which is typically a qualitatively reasonable approximation in these cases, sheath boundary conditions permit a SOL interchange mode with no line bending penalty that only sees bad curvature

(double null case), while the boundary condition that pertains in the edge requires either averaging over both good and bad curvature or line bending to avoid the good curvature.

These results show that the SOL of a limited plasma is subject to a number of instabilities which are either not present or are weaker in an equivalent diverted plasma. In the latter case, the X-point effectively isolates the modes from the (typically destabilizing) sheath boundary condition at the plates.

V. Conclusions

The main result of this paper is that there is a synergism between resistivity and X-point geometry. The dramatic enhancement of $k_\perp$ near the X-points in the presence of resistivity (or electron inertia) leads to a disconnection of eigenmodes across the X-point region, and this in turn allow a fast growing, moderate-n instability, the resistive X-point mode. The RX mode is the basic unstable mode in the resistive L-phase boundary plasma of a diverted tokamak. It is naturally localized to the bad curvature region by upper and lower X-points in a double null configuration (even when one of the nulls in deep in the SOL). The present work together with that of recent BOUT code analyses suggests that it is important for turbulent transport.

Resistive X-point effects exist over a wide range of plasma parameters and mode numbers. As parameters approach the ideal ballooning instability limit, the RX mode transforms into the ideal mode, while for very resistive parameters, the RX mode transforms into the resistive strong ballooning mode.

Limited and diverted plasmas are found to have different edge stability properties. In particular, robust sheath related instabilities in the limiter plasma case are mitigated in divertor plasmas by the X-point disconnection effect. For divertor plasmas, the edge and SOL are similar, because of the same disconnection effect.

The present linear calculations for L-mode plasmas in divertor geometry and the corresponding BOUT simulations[14,15] share the following features: i) robustly unstable moderate-to-low-n curvature driven modes localized by the X-points, ii) similar edge and SOL stability properties, iii) qualitatively similar scalings in growth rate with curvature, electron collisionality and electron skin depth, and iv) comparing a limited configuration with the diverted one, increased instability in the SOL.

The synergism between X-point geometry and resistivity is the crucial point in understanding all of these important features. The success of the BOUT code in realistic simulation of experiments with respect to the cross-field transport in L and H phases, the spontaneous generation of radial electric fields, sheared flow and an L-H like transition is a hopeful sign that the physics models employed in these calculations contain the key ingredients for understanding edge turbulence in tokamaks. The present work suggests that the magnetic geometry of the boundary plasma is an important experimental knob for controlling edge turbulence and influencing global confinement.

Acknowledgments

The authors wish to thank G.D. Porter and R. Moyer for providing boundary plasma profile and magnetic geometry data for DIII-D, and D. Ryutov for stimulating and informative conversations. This work was supported by the U.S. Department of Energy (DOE) under contract/grant numbers DE-FG03-97ER54392, and W-7405-ENG-48; however this support does not constitute an endorsement by the DOE of the views expressed herein.

Appendix A: Limiting Cases of $\chi_{||}$

In the $\chi_{||} = 0$ or ideal, convective limit of Eq. (12) was treated in the main text and gives

$$T_1 = \frac{\omega_{*eT}}{\tilde{\omega}} \phi_1 . \tag{A1}$$

Here we consider the opposite case of $\chi_{||} = \infty$, which corresponds to setting

$$\delta(\nabla_{||} T_e) = 0, \tag{A2}$$

where it is important that the unit vector **b** be perturbed. Substituting for $A_{||}$ and $J_{||}$ in terms of ϕ_1, one obtains the result

$$T_1 = \frac{\omega_{*eT}}{\tilde{\omega}} \left[\frac{\tilde{\omega} - \omega_{*en} + k_\perp^2 \rho_s^2 (\tilde{\omega} - \omega_{*i})}{\tilde{\omega} - \omega_{*en} + i\omega_\eta + \tilde{\omega} H} \right] \phi_1 . \tag{A3}$$

The term in square brackets is essentially $\delta J_{||}$, and corresponds to the ideal expression except that all the ω_{*eT} terms are missing. The electrostatic limit (ω_η/ω or H large) gives $T_1 = 0$ as can be deducted directly from Eq. (A2). When employed in the ballooning equation, this limit effectively turns the electron temperature gradient off, and typically results in a somewhat reduced ballooning drive, which depends on the total pressure gradient. The fundamental character of the RX modes is not affected. Finally for sufficiently small $k_\perp$ (low-n), the term in square brackets becomes unity, and remarkably the result is the same as Eq. (A1) obtained when $\chi_{||} = 0$.

Appendix B: Gyrokinetic ion model

In this Appendix, we present a brief derivation of the gyrokinetic ion model employed in Sec. IV A.

Of the fundamental linear set given by Eqs. (9) – (12), only Eqs. (9) and (11) involve ion physics. As written, the continuity equation, Eq. (11) is for ions. It is also possible to write down the electron continuity equation. Then, the vorticity equation, Eq. (9), is obtained from quasineutrality, $n_i = n_e$. Thus, to generalize the ion model from a

fluid model to a gyrokinetic one, it is only required to derive a gyrokinetic version of the ion continuity equation.

Following Lee and Catto,[26] we first extract the adiabatic piece of the perturbed ion distribution function f by setting

$$f = -\frac{Ze\Phi}{T_i} f_0 \exp(ia\sin\theta) + g \tag{B1}$$

where f_0 is the Maxwellian equilibrium distribution function, Φ is the perturbed potential, $a = k_\perp v_\perp/\Omega$ and $\Omega = eB/m_i c$. The gyrokinetic equation for g then becomes

$$(\omega - \omega_d) g = \omega\left(\frac{Ze\Phi}{T_i} f_0 J_0 - J_0\, \xi\cdot\nabla f_0\right) \tag{B2}$$

where $\omega_d = \mathbf{k}\times\mathbf{b}\cdot[(v_\perp^2/2\Omega)\nabla\ln B + (v_\parallel^2/\Omega)\kappa]$, $J_0 = J_0(a)$ is a Bessel function, $\xi = (c\Phi/\omega B)\,\mathbf{k}\times\mathbf{b}$, and we have assumed $v_\parallel\nabla_\parallel << \omega_d$. Also, in this Appendix we work in the E×B drift frame. The perturbed ion density takes the form

$$n = \frac{n_0 Ze\Phi}{T_i}\left(-1 + \int d^3v\, J_0^2 f_0 \frac{\omega - \omega_{*in} - (v^2/2v_i^2 - 3/2)\omega_{*iT}}{\omega - \omega_d}\right) \tag{B3}$$

The above result is also consistent with the low frequency limit of the general frequency gyrokinetic result.[27] Approximating ω_d by its thermal value in the integral, $\omega_d \approx \omega_{\kappa i}$ yields the ion continuity equation

$$(\tilde{\omega} - \omega_{\kappa i}) n_1 = \left\{\omega_{\kappa e} + \omega_{*en} - \frac{T_e}{T_i}\left[(\tilde{\omega} - \omega_{*in})(1 - \Lambda_0) - \omega_{*iT} b(\Lambda_0 - \Lambda_1)\right]\right\}\phi_1 \tag{B4}$$

where $b = k_\perp^2\rho_i^2$, $\Lambda_n = \Lambda_n(b) = I_n(b)e^{-b}$, I_n is a Bessel function, we have reverted to the notation of the main text [viz., $n_1 = n/n_0, \phi_1 = (T_i/T_e)(Ze\Phi/T_i)$], transformed back to the lab frame ($\omega \to \tilde{\omega}$), and noted that $\omega_{*in}/T_i = -\omega_{*en}/T_e$ and $\omega_{\kappa i}/T_i = \omega_{\kappa e}/T_e$. In obtaining Eq. (B4) the following identities have also been used

$$\int_0^\infty dx\, e^{-x^2/2} J_n^2(b^{1/2}x) = \Lambda_n(b)\,, \tag{B5}$$

$$\frac{1}{2}\int_0^\infty dx\, x^3 e^{-x^2/2} J_n^2(b^{1/2}x) = b\Lambda_{n+1}(b) - (b-n-1)\Lambda_n(b)\,. \tag{B6}$$

Equation (B4) is the desired gyrokinetic generalization of Eq. (11). It may be verified that the b << 1 expansion of Eq. (B4) reduces to Eq. (11), where $\omega_{*i} \equiv \omega_{*in} + \omega_{*iT}$. The straight-field-line limit of Eq. (B4) is also consistent with Pegoraro and Schep.[28]

References

[1] B.N. Rogers, J.F. Drake and A. Zeiler, Phys. Rev. Lett. 81, 4396 (1998).

[2] B. Scott, in *Theory of Fusion Plasmas*, 1998, proc. of the *Joint Varenna-Lausanne International Workshop* (Società Italiana di Fisica, Bologna, 1998), p. 359.

[3] D. Farina, R. Pozzoli and D.D. Ryutov, Nucl. Fusion **33**, 1315 (1993).

[4] N. Mattor and R.H. Cohen, Phys. Plasmas **2**, 4042 (1995).

[5] J.R. Myra and D. A. D'Ippolito, Phys. Plasmas **5**, 659 (1998).

[6] C.M. Bishop, P. Kirby, J.W. Connor, R.J. Hastie and J.B. Taylor, Nucl. Fusion **24**, 1579 (1984); C.M. Bishop, Nucl. Fusion **26**, 1063 (1986); **27**, 1765 (1987).

[7] C.C. Hegna and J.D. Callen, Phys. Plasmas B **4**, 3031 (1992).

[8] W. Kerner, O. Pogutse, R. Van der Linder, Plasma Phys. Cont. Fusion **39**, 757 (1997).

[9] H.R. Wilson, Plasma Phys. Cont. Fusion **33**, 221 (1991).

[10] T.S. Hahm and P.H. Diamond, Phys. Fluids **30**, 133 (1987).

[11] J.R. Myra, D. A. D'Ippolito and J.P. Goedbloed, Phys. Plasmas **4**, 1330 (1997).

[12] A.V. Nedospasov, Fiz. Plazmy **15**, 1139 (1989) [Sov. J. Plasma Phys. **15**, 659 (1989)].

[13] J.R. Myra, D.A. D'Ippolito, X.Q. Xu and R.H. Cohen, Contrib. Plasma Phys. **40**, 352 (2000).

[14] X.Q. Xu, R.H. Cohen, T.D. Rognlien and J.R. Myra, Phys. Plasmas **7**, 1951 (2000).

[15] X.Q. Xu, R. H. Cohen, G.D. Porter, T.D. Rognlien, D.D. Ryutov, J.R. Myra. D.A. D'Ippolito and R. Moyer, Nucl. Fusion **40** Yokohama Special Issue 3, 731 (2000).

[16] J.R. Myra, D.A. D'Ippolito, X.Q. Xu and R.H. Cohen, Phys. Plasmas **7**, xxx (2000).

[17] A. Zeiler, J.F. Drake, B. Rogers, Phys. Plasmas **4**, 2134 (1997).

[18] X.Q. Xu and R.H. Cohen, Contrib. Plasma Phys. **38**, 158 (1998).

[19] H.L. Berk, R.H. Cohen, D.D. Ryutov, Yu.A. Tsidulko and X.Q. Xu, Nucl. Fusion **33**, 263 (1993), and refs. therein.

[20] R.H. Cohen and D.D. Ryutov, Phys. Plasmas **2**, 2011 (1995).

[21] D. Farina, R. Pozzoli and D.D. Ryutov, Plasma Phys. Contol. Fusion **35**, 1271 (1993).

[22] L.L. Lao, J.R. Ferron, R.J. Groebner, W. Howl et al., Nucl. Fusion **30**, 1035 (1990).

[23] R.A. Moyer, R. Lehmer, J.A. Boedo, J.G. Watkins, et al., J. Nucl. Mat. **266**-**269**, 1145 (1999).

[24] see for example T.C. Hender, B.A. Carreras, W.A. Cooper, J.A. Holmes, P.H. Diamond, and P.L. Similon, Phys. Fluids **27**, 1439 (1984); and refs. therein.

[25] S.V. Novakovskii, P.N. Guzdar, J.F. Drake and C.S. Liu, Phys. Plasmas **2**, 3764 (1995).

[26] X.S. Lee and P.J. Catto, Phys. Fluids **24**, 2010 (1981); P.J. Catto, W.M. Tang and D.E. Baldwin, Plasma Phys. **23**, 639 (1981).

[27] X.S. Lee, J.R. Myra and P.J. Catto, Phys. Fluids **26**, 223 (1983), Eqs. (30) and (31).

[28] F. Pegoraro and T.J. Schep, Phys. Fluids **24**, 478 (1981).

Figure captions

1. Variation of k_θ and k_ψ along a field line for a single null X-point geometry with X-point at $\theta = 0, 2\pi$. The case shown is for $\theta_0 = \pi$, viz. $k_\psi(\pi) = 0$.
2. Variation of $k_\perp^2$ along a field line (top) and corresponding eigenfunctions (bottom) for three cases, showing progressive disconnection because of resistive X-point effects. The first case (solid) has $Z_{eff} = 0$ and d = 2.8 cm where d is midplane distance from the separatrix in the SOL. The second case (dashed) has $Z_{eff} = 2$ and d = 2.8 cm, while the third case (dotted) has $Z_{eff} = 2$ and d = 1.0 cm. In all three cases the eigenfunctions are larger in the bad curvature region ($0 < \theta < \pi$) than in the good curvature region ($\pi < \theta < 2\pi$).
3. a) Normalized resistive frequency along a field line (note the logarithmic scale) and b) corresponding eigenfunction (solid) and Poynting flux (dotted) for an RX mode in the edge plasma (reprinted from Ref. 16).
4. Typical unstable spectrum for L-mode parameters showing growth rate vs. toroidal mode number. The RX, classical and drift-Alfvén contributions to the spectra are shown. For the parameters of this figure, $\gamma = 200 \times 10^3\ s^{-1}$ corresponds to $\gamma/\gamma_{mhd0} = 0.26$ and n = 300 to $k_{\theta 0}\rho_s = 0.75$.
5. Contours of growth rate γ vs. edge density and temperature with inset eigenfunctions $\psi(\theta)$ (in the extended ballooning coordinate range $-4 < \theta < 7$) for the four extreme corners of the parameter space. The upper right corner is the regime of ideal strong (IS) ballooning instability; the lower right corner is resistive strong (RS) ballooning; and the remainder of the diagram is the regime of resistive X-point (RX) effects.
6. Comparison of unstable spectra for the fluid and gyrokinetic ion models on a field line just inside the separatrix where the enhancement of $k_\perp$ is the strongest.
7. Growth rate scaling with a) curvature κ, b) collisionality ν_e, and c) electron beta β_e or inverse skin depth squared ($\beta_e = \rho_s^2 / \delta_e^2$). The two curves show the scaling of the

high-n (classical, upper dashed curve) and low-n (RX, lower solid curve) branches. In each case, κ, ν_e and β_e are varied about their base case L-mode values, indicated by arrows.

8. Comparison of unstable spectral for limited and diverted plasmas in a) the edge and b) the SOL . The X-point or diverted plasma spectrum is shown with the symbol "x"; the limited or shifted circle model plasma spectrum is shown with the circle symbol "o" (reprinted from Ref. 16).
9. Comparison of eigenfunctions in the edge for the limited (circle) and diverted (X-point) cases. In a) the eigenfunctions are shown in the extended ballooning coordinate ($-\infty < \theta < \infty$); in b) they have been mapped back onto the periodic variable $0 \le \theta \le 2\pi$.

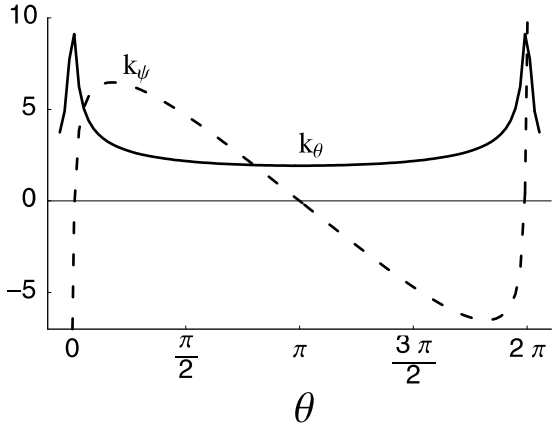

Fig. 1

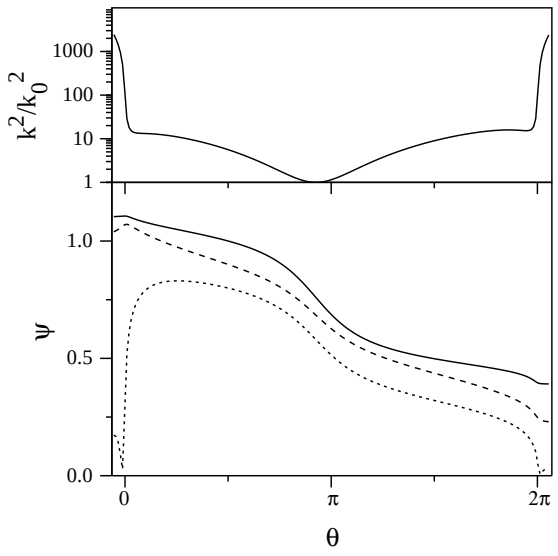

Fig. 2

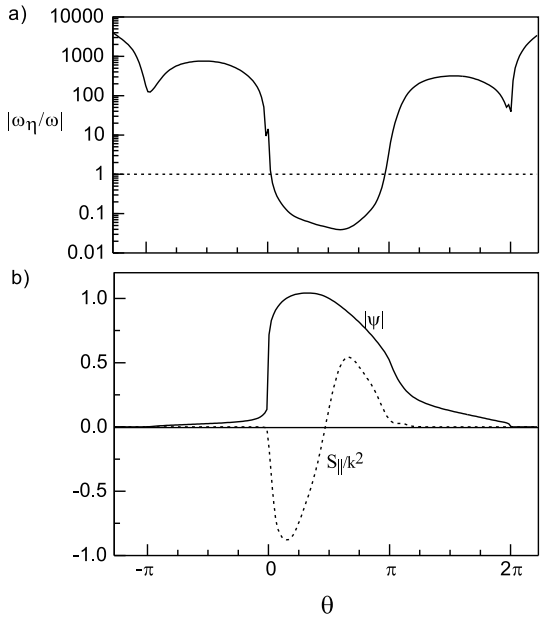
a)
10000
1000
100
10
1
0.1
0.01
|ωη/ω|
b)
1.0
0.5
0.0
-0.5
-1.0
|ψ|
S||/k2
-π
0
π
2π
θ

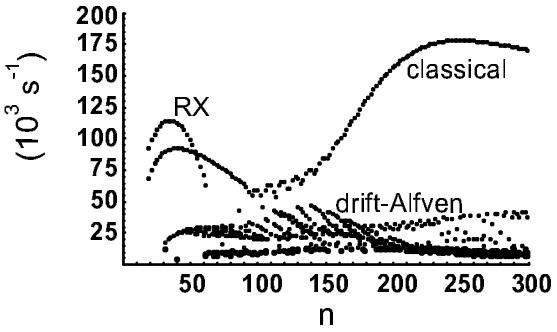
200
175
150
125
100
75
50
25
$(10^3\ s^{-1})$
RX
classical
drift-Alfven
50
100
150
200
250
300
n

Fig. 4

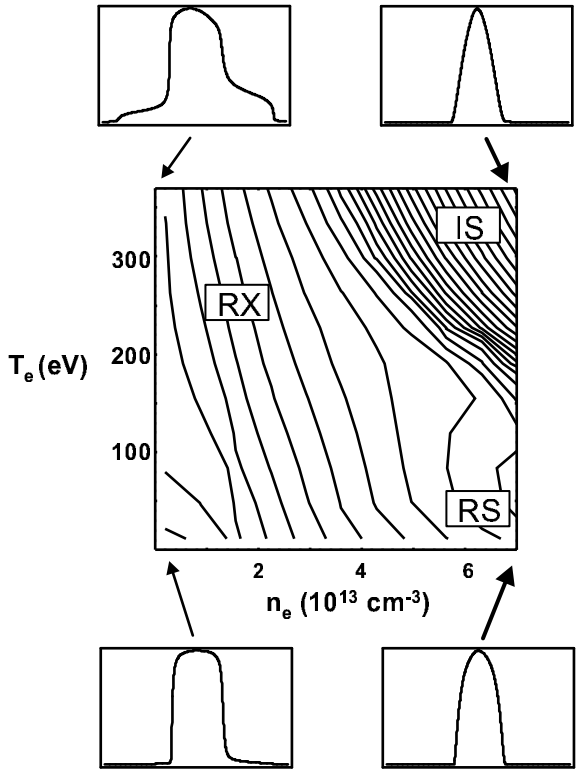

Fig. 5

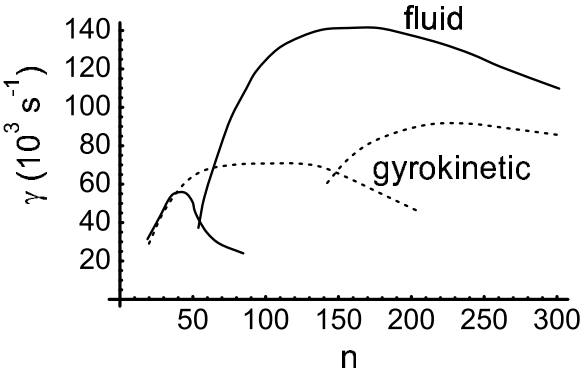
fluid
gyrokinetic
140
120
100
80
60
40
20
50
100
150
200
250
300
n
γ (10^3 s^-1)

Fig. 6

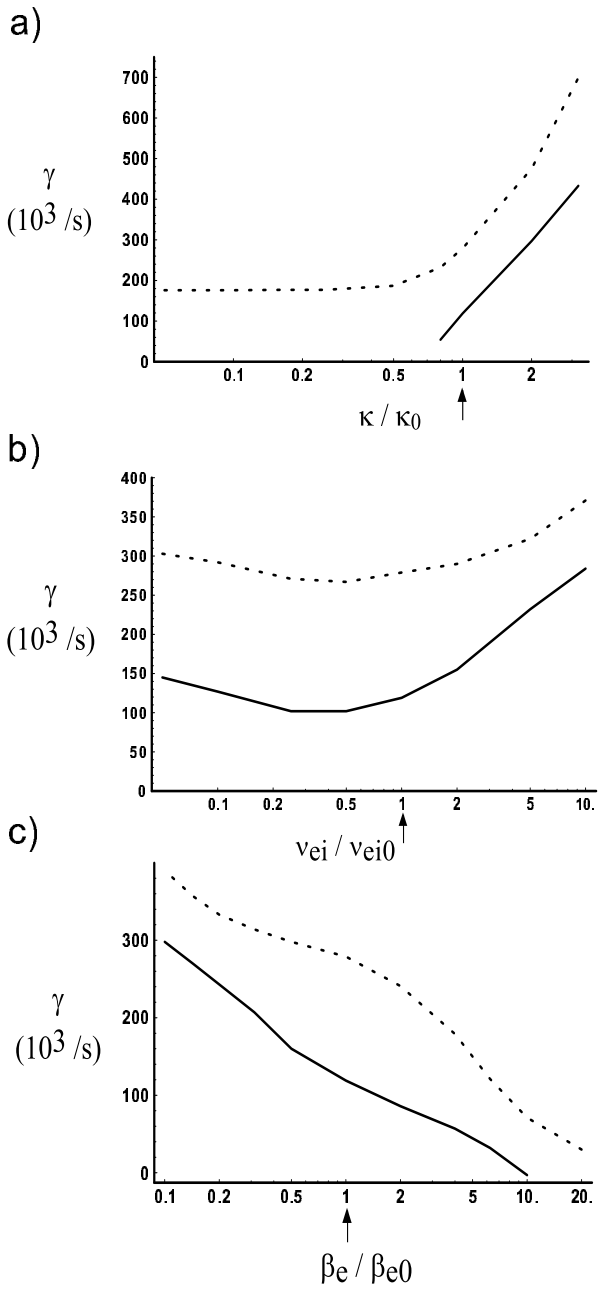
a)
γ
(10^3 /s)
700
600
500
400
300
200
100
0
0.1
0.2
0.5
1
2
κ / κ0
b)
γ
(10^3 /s)
400
350
300
250
200
150
100
50
0
0.1
0.2
0.5
1
2
5
10.
νei / νei0
c)
γ
(10^3 /s)
300
200
100
0
0.1
0.2
0.5
1
2
5
10.
20.
βe / βe0

Fig. 7

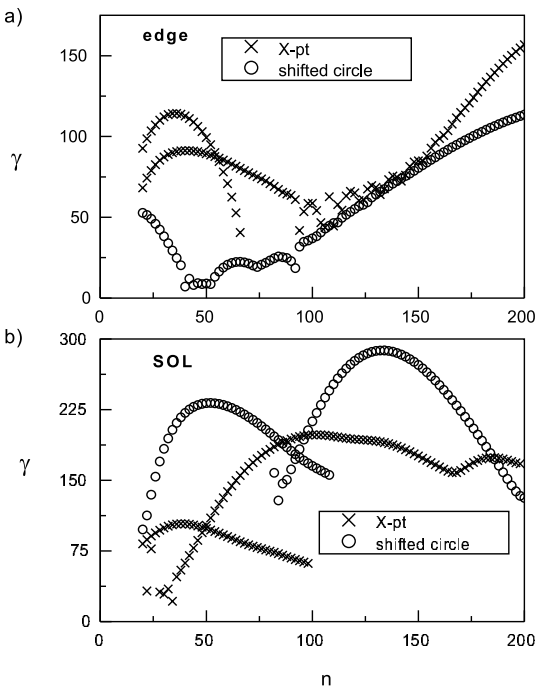
a)
edge
X-pt
shifted circle
γ
150
100
50
0
0
50
100
150
200
b)
SOL
γ
300
225
150
75
0
X-pt
shifted circle
n

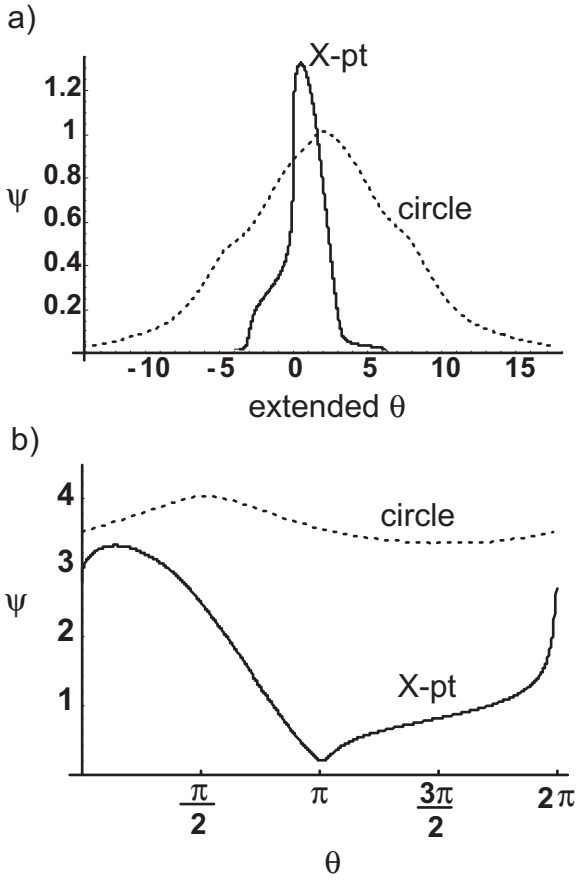
a)
X-pt
1.2
1
0.8
ψ
0.6
0.4
0.2
circle
-10
-5
0
5
10
15
extended θ
b)
4
3
ψ
2
1
circle
X-pt
π/2
π
3π/2
2π
θ

Fig. 9